



Boosting the photocatalytic properties of NaTaO₃ by coupling with AgBr

F. Puga¹ · J. A. Navío¹ · M. C. Hidalgo¹

Received: 19 May 2022 / Accepted: 25 October 2022 / Published online: 10 November 2022
© The Author(s) 2022

Abstract

AgBr/NaTaO₃ composites, with different molar % of NaTaO₃ (Br/NTO(X%)), have been synthesized by simple precipitation methods; bare NaTaO₃ was synthesized by hydrothermal procedure, while AgBr was synthesized by a precipitation procedure using cetyl-tri-methyl-ammonium bromide (CTAB) and AgNO₃. Samples have been characterized by X-ray diffraction (XRD), N₂ adsorption, UV–vis diffuse reflectance spectroscopy (DRS), Fourier-transform infrared spectroscopy (FT-IR), Transmission electron microscopy (TEM) and X-ray photoelectron spectroscopy (XPS). Photocatalytic activity of the as-prepared photo-catalysts was evaluated through photocatalytic degradation of rhodamine B (RhB), methyl orange (MO) and caffeic acid (CAFA) under UV and visible illumination. Single AgBr material and Br/NTO(X%) composites displayed the ability to absorb light in the visible region, while NaTaO₃ is only photoactive under UV irradiation. Based on the position of conduction and valence bands of AgBr and NaTaO₃, the heterojunction between these two photo-catalysts corresponds to a type II junction. In the case of photocatalytic degradation of RhB and CAFA, Br/NTO(x%) composites have highest photocatalytic activity than that obtained by both parental materials under the same operational conditions. AgBr and Br/NTO(x%) composites achieve a fast degradation of MO, together with a considerable adsorption capacity, attributed to the presence of a remaining amount of residual CTAB on the AgBr surface. In summary, coupling AgBr with NaTaO₃ improves the photocatalytic activity under both UV and visible illumination with respect to the parental components, but the performance of the composites is highly dependent on the type of substrate to be degraded and the illumination conditions.

Keywords Sodium tantalite · AgBr · Photo-catalysis · Dyes · Caffeic acid

1 Introduction

Heterogeneous photo-catalysis, an environmentally friendly advanced oxidation process (AOP), has gradually provided a stage for environmental remediation. This technology has many advantages, like the use of solar light (a sustainable resource), a fast reaction rate and low energy consumption [1, 2]. Several semiconductors (like TiO₂, ZnO, ZnS, ZrO₂, MoS₂, WO₃, SnO₂, Fe₂O₃, CdS, etc.) can be used as a

photo-catalyst for pollutant remediation in aqueous media. TiO₂ is the most widely studied photo-catalyst, due to its high stability, nontoxicity, cost-effectiveness, among other features. However, there are some drawbacks, like the fast recombination rate of photo-generated electron–hole pairs and the fact that it is only photoactive by UV radiation [3–5].

In the last decades, a wide range of photo-catalysts has been developed [6], including semiconductors with perovskite structure. Perovskites comprise a large group of compounds with great flexibility in terms of their possible applications, since almost all the elements of the periodic table can be used as substitutes to prepare systems with this type of structure. In particular, perovskite-structured tantalates have gained significant attention [7–9], thanks to their chemical stability, nontoxicity and photocatalytic activity [10]. Among tantalate photo-catalysts, sodium tantalate (NaTaO₃) is a stable semiconductor, with a layered structure and efficient charge separation, which makes it a promising photocatalytic material [11]. However, NaTaO₃ is not active

✉ F. Puga
felipe.puga.martinez@gmail.com

✉ J. A. Navío
navio@us.es

M. C. Hidalgo
carmen.hidalgo@csic.es

¹ Instituto de Ciencia de Materiales de Sevilla (ICMS), Centro Mixto, Universidad de Sevilla-CSIC, Américo Vespucio 49, 41092 Seville, Spain

under visible light irradiation and has a high recombination rate of photo-generated electron–hole pairs, which renders this semiconductor a poor performer in the photocatalytic degradation of pollutants [12]. Therefore, numerous studies have been carried out to improve the photo-activity of this semiconductor in the visible region [10, 13].

Silver bromide (AgBr) is an important plasmonic photocatalyst with a narrow band gap (2.6 eV), which has attracted considerable research attention due to its high photocatalytic activity in the visible region as it is a photo-sensitive material [14]. Nevertheless, there are certain difficulties in the practical application of pristine AgBr which have been outlined in a recent review article, mainly associated to photo-corrosion/photo-instability and large size for AgBr particles [15]. However, it should be noted that, due to the proper location of the valence band (VB) and conduction band (CB), AgBr is a good candidate to be easily coupled with other semiconductors for the development of coupled systems, as reported in [16] and in some of its references related to AgBr coupling; moreover, this feature is accepted in the conclusions of the review paper [15], suggesting further study of AgBr with rational design and modifications to understand and improve the properties of AgBr for coupling with other semiconductors.

So far, most of the research for the synthesis of AgBr has focused on issues, such as the effects of reagent ratio, synthesis temperature, etc. However, very little attention has been paid to the question of silver source selection. In this scenario, it should be highlighted, the novel results of an AgBr-based nanomaterial, synthesized by Tollen's reagent with the aid of hexa-decyl-tri-methyl-ammonium bromide (CTAB), which showed excellent affinity to anionic species and was used for the removal of organic dyes in aqueous solutions [17].

On the basis of the aforementioned, the objective of this work is to develop coupled AgBr/NaTaO₃ photo-catalysts with different molar percentages of NaTaO₃, to explore their features as composite materials for heterogeneous photocatalysis. Silver bromide (AgBr) has been prepared by a surfactant-assisted synthesis method with hexa-decyl-tri-methyl-ammonium bromide (CTAB). The surfactant acts as a source of bromide ions and as a stabilizing agent. With these ideas, the coupling of an AgBr–CTAB with a NaTaO₃ and the consequences that the CTAB-assisted AgBr synthesis method provides to the photocatalytic properties of the coupled AgBr/NaTaO₃ system will be explored for the first time. The synthesized compounds, as well as the parent materials, AgBr and NaTaO₃, were fully characterized by different techniques and, afterward, their photocatalytic activities were evaluated by testing, under two illumination conditions (UV and visible), the degradation of three selected substrates: rhodamine B (RhB), methyl orange (MO) and caffeic acid (CAFA).

In the context of this study, it should be noted that, to date and to the best of our knowledge, there are no studies on the coupling of AgBr with NaTaO₃. In this case, our results may provide new ideas for the development of composite materials, especially using the NaTaO₃ photo-catalyst.

2 Experimental procedures and techniques

2.1 Sample preparation

NaTaO₃ synthesis: 0.663 g of tantalum(V) oxide (Ta₂O₅, Alfa Aesar, 99%) was mixing with 60 mL of NaOH 0.75 M, and the suspension was placed in ultrasound for 15 min and then stirred for 60 min. After that, the suspension was reacted hydrothermally at 200 °C for 24 h. Subsequently, the precipitate was separated by filtration and washed with portions of deionized water. Finally, the NaTaO₃ powder was dried at 100 °C for 24 h.

AgBr synthesis: 0.283 g of AgNO₃ was dissolved in 10 mL of deionized water, and 0.717 g of CTAB (Cetyltrimethylammonium bromide/Sigma-Aldrich) was dissolved in 50 mL of deionized water. Then, the AgNO₃ solution was mixed (drop by drop) with the CTAB solution (molar ratio CTAB/AgNO₃ = 1.18), and the resulting suspension was shielded from the light and stirred for 24 h. After that, the precipitate was separated by filtration and washed with several portions of deionized water and ethanol. Finally, the AgBr powder was dried at 75 °C for 24 h.

Synthesis of the AgBr/NaTaO₃ composite: The coupling was performed by precipitation-deposition of AgBr on NaTaO₃ already synthesized, taking into account the selected values for the AgBr/NaTaO₃ ratio (100 mol AgBr/X mol NaTaO₃). For this purpose, the same procedure of AgBr synthesis was used, except that a certain amount of NaTaO₃ synthesized above was added to the AgNO₃ solution, before mixing with the CTAB solution. The prepared coupled samples (AgBr/NaTaO₃) will be referred to hereafter, according to their corresponding nominal molar percentages, as Br/NTO(X %), where X are 20, 50 or 75. In the synthesis of all this coupled samples, the CTAB/AgNO₃ molar ratio, and the concentration of AgNO₃ and CTAB solutions was always the same used in the AgBr synthesis.

2.2 Characterization of the samples

The crystalline structure of as-prepared samples was investigated by powder X-ray diffraction (XRD). XRD patterns were obtained on an X'PertPro Panalytical instrument with Cu K α radiation (40 mA, 45 kV, and $\lambda = 1.5406 \text{ \AA}$) at ambient temperature. Peaks were fitted using a Voigt function. Specific surface area (S_{BET}) measurements were carried out at low-temperature N₂ adsorption using a Micromeritics

ASAP 2010 instrument. Before the analysis, the samples were degasified at 150 °C for 30 min in a helium flow. For pore size distribution, the Barrett–Joyner–Halenda (BJH) model was used. Diffuse Reflectance Spectroscopy (DRS) was carried out to analyze the optical absorption properties of the samples. The spectra were performed on a Cary 300 spectrophotometer equipped with an integrating sphere, using BaSO₄ as reference. The indirect optical band gap was estimated by the Tauc plots, following the steps of the procedure reported in [18]. The morphology of the samples was studied by S/TEM in a Talos™ F200S FEI microscope. The XPS analyses were carried out on a Leybold-Heraeus LHS-10 spectrometer, working at a constant path energy of 50 eV and at a pressure below 2×10^{-9} Torr. This device includes an EA-200MCD hemispheric electron analyzer with a dual X-ray source working with Al K α ($h\nu = 1486.6$ eV) at 120 W and 30 mA. The C 1 s signal at 284.6 eV of adventitious carbon was chosen as the internal energy reference. Samples were previously degassed in the pre-chamber of the instrument at 150 °C at a pressure below 2×10^{-8} Torr to eliminate the adsorbed chemical water. Fourier-Transform Infrared Spectrometer (FTIR) was used to identify functional groups of the samples. The FTIR spectra were recorded in transmission mode with a JASCO FT/IR-6200 IRT-5000 spectrometer.

2.3 Photocatalytic activity tests

The evaluation of the photocatalytic activity of the samples was performed using two illumination conditions, UV and visible, by following the degradation reactions of rhodamine B (RhB), methyl orange (MO) and caffeic acid (CAFA). Rhodamine B, methyl orange and caffeic acid were supplied by Sigma-Aldrich (all Reagent Plus $\geq 95\%$). Details and experimental conditions are reported in the following references. [19, 20]. In summary, 100 mg of photo-catalyst was added to 100 mL of substrate solution (10 ppm RhB, 20 ppm MO or 10 ppm CAFA) under constant bubbling of air to keep the reaction mixture homogenous. UV–visible spectroscopy with a Cary 100 (Varian) spectrometer was used to evaluate the concentration of each substrate, considering the main peak of each compound, located at 554 nm (for RhB), 465 nm (for MO) and 312 nm (for CAFA). Every experiment was performed at least twice to ensure reproducibility, the standard deviation being 5%. Two types of blank tests were performed: (i) under illumination without catalyst and (ii) with catalysts in the dark. From these tests, it was confirmed that the combination of catalyst and illumination are prerequisites for the photocatalytic degradation process under our experimental conditions.

Silver content was analyzed in the medium after prolonged UV illumination by Atomic Emission Spectrometry with plasma ICP (SpectroBlue T1 equipment), whereas

bromide, under the same conditions, was determined by ion chromatography (Metrohm 930 Compact IC flex equipment).

3 Results

3.1 Characterization and physicochemical properties

Figure 1 shows the X-ray diffraction (XRD) patterns for the single materials (AgBr and NaTaO₃) and two selected of the composite materials, Br/NTO(20%) and Br/NTO(50%). NaTaO₃ present a XRD pattern that correspond to a monoclinic phase (JCPDS 01-074-2478), while AgBr exhibit a XRD pattern belonging to a cubic phase (JCPDS 01-079-0149). In the diffractogram of single NaTaO₃, there are some small peaks (marked with green diamonds) that do not correspond to the aforementioned JCPDS sheet. These peaks are attributed to Na₂Ta₂O₆ with a cubic crystal structure (JCPDS 01-070-1155). According to a reference [21], Na₂Ta₂O₆ corresponds to an intermediate phase within an

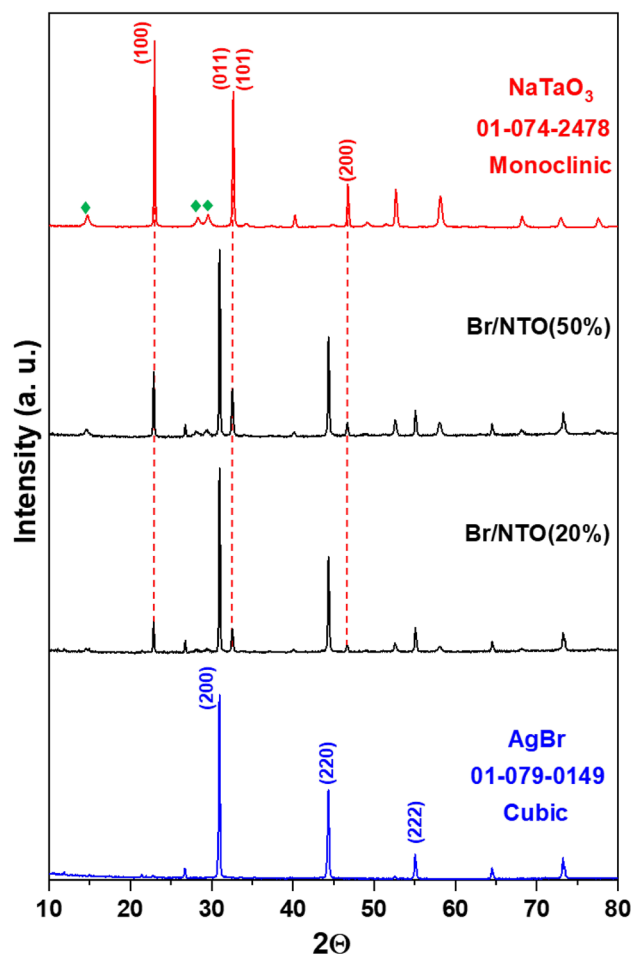


Fig. 1 XRD patterns of the synthesized samples

indirect reaction route for the formation of NaTaO_3 from Ta_2O_5 . Thus, $\text{Na}_2\text{Ta}_2\text{O}_6$ corresponds to a metastable phase, while NaTaO_3 is a thermodynamically stable phase [22]. Despite all this, although the presence of $\text{Na}_2\text{Ta}_2\text{O}_6$ together with NaTaO_3 is evident from XRD results, according to our calculations, $\text{Na}_2\text{Ta}_2\text{O}_6$ only corresponds to 3% by weight, so, in practical terms, it can be said that the synthesis of an almost pure NaTaO_3 was obtained.

In the diffractograms of the coupled samples, the main peaks corresponding to AgBr (planes 200, 220 and 222) and NaTaO_3 (planes 100, 011, 101 and 200) can be clearly seen. In addition, no peaks other than that for AgBr and NaTaO_3 structures mentioned (except $\text{Na}_2\text{Ta}_2\text{O}_6$) were detected, so the formation of the AgBr/ NaTaO_3 composites was successfully obtained. Additionally, it can be observed in the coupled samples that, as the amount of NaTaO_3 in the composite increases, the intensity of its peaks also increases.

The crystallite size of the prepared samples was estimated from the widening of their XRD main peaks using the well-known Scherrer formula. The main crystalline sizes of pristine materials (AgBr or NaTaO_3) and AgBr/ NaTaO_3 coupled systems are compiled in Table 1, along with other

physicochemical parameters. As can be seen, the primary crystallite size for both pristine samples undergoes significant changes in the coupled samples, indicating that the coupling of these materials generates changes in the estimation of the average crystallite sizes. A first analysis of the crystallite size results in Table 1 indicates that for low percentages of NaTaO_3 , there is a change in the crystallite sizes of the pristine samples. Thus, after the coupling of both samples, it is observed that while for NaTaO_3 , the crystallite size decreases, for AgBr, it increases, reaching a minimum for the AgBr/ NaTaO_3 (75%) sample; these results could be related to the generation of crystalline defects after the coupling of NaTaO_3 and AgBr.

N_2 adsorption/desorption analysis was performed to determine the specific surface area (by BET method) and pore diameter distribution (by BJH method) of NaTaO_3 and AgBr/ NaTaO_3 composites samples. In Fig. 2A, the isotherm of NaTaO_3 is presented separate from the Br/NTO(75%) and/or Br/NTO(50%), because the quantity of the adsorbed volume in NaTaO_3 is much greater than that corresponding to the two composite. As can be seen in Fig. 2A, NaTaO_3 and Br/NTO(75%) have a type IV isotherm, with a type IV

Table 1 Physicochemical parameters of the indicated samples

Sample	S_{BET} (m^2/g)	E_g (eV)	Crystallite size $D_{\text{AgBr (200)}}$ (nm)	Crystallite size $D_{\text{NaTaO}_3 (100)}$ (nm)
AgBr	< 1	2.59	343	–
Br/NTO(20%)	< 1	2.54	412	165
Br/NTO(50%)	1.79	2.51	284	169
Br/NTO(75%)	3.68	2.46	183	169
NaTaO_3	34.5	3.77	–	253

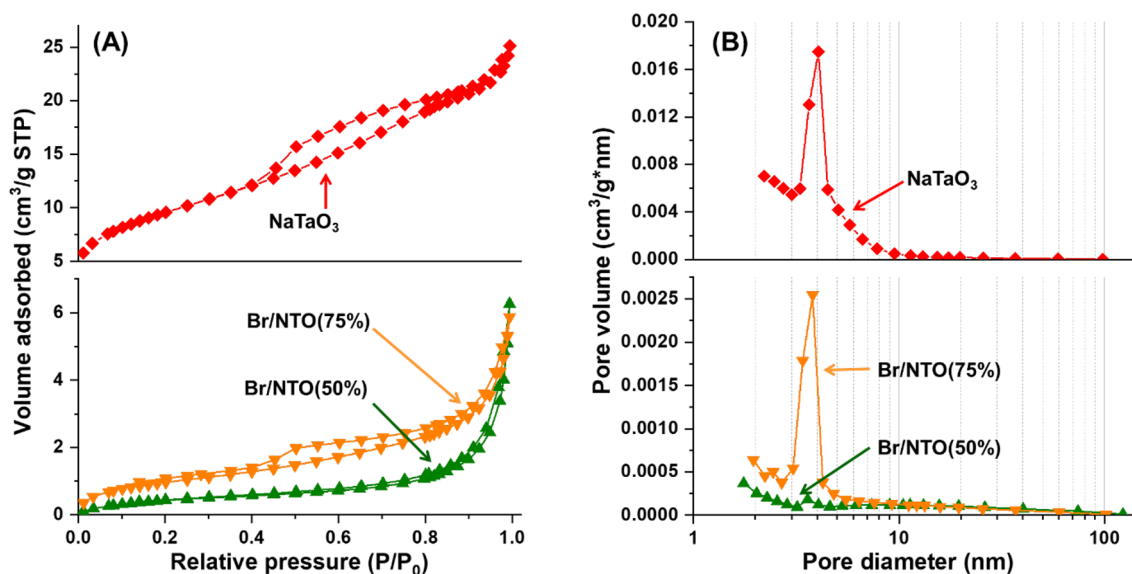


Fig. 2 N_2 adsorption–desorption isotherms (A) and pore size distribution (B) of the samples NaTaO_3 , Br/NTO(50%) and Br/NTO(75%)

hysteresis loop, indicating that these materials are of the mesoporous type, with slit-like pores [23]. On the other hand, Br/NTO (50%) has a type III isotherm, according to the IUPAC classification, which indicates that this material probably has a low adsorption capacity. The specific surface areas of the synthesized materials are shown in Table 1. According with the results, single AgBr and the Br/NTO(20%) composite have a very low surface area ($S_{\text{BET}} < 1 \text{ m}^2/\text{g}$); but, for Br/NTO(50%) and Br/NTO(75%) samples, the specific surface increases with the increment of the molar content of NaTaO_3 in the composites.

The pore size distribution of Br/NTO(50%), Br/NTO(75%) and NaTaO_3 is shown in Fig. 2B. The pore size distribution of NaTaO_3 is presented separate from the Br/NTO(75%) and/or Br/NTO(50%) by the same reason as before (quantity of pore volume in this case). As can be seen, the pore size distribution profiles of NaTaO_3 and Br/NTO(75%) are very similar, with pore diameters between 2 and 100 nm, concentrating between 3 and 5 nm. This corroborates the condition of being mesoporous materials, as mentioned above. In the case of the Br/NTO(50%) sample, it also has pore diameters between 2 and 100 nm, but it does not have the population distribution between 3 and 5 nm observed for the NaTaO_3 and Br/NTO(75%) samples.

Figure 3 shows the UV–Vis DRS spectra of AgBr, NaTaO_3 and the coupled samples. AgBr has a wide absorption region, started from 500 to 270 nm; in contrast, the absorption edge of single NaTaO_3 is about 370 nm and only absorb in the UV region. Compared with NaTaO_3 , all the coupled samples have the ability of absorb visible light. The band gap values have been estimated by means of Tauc plots and are compiled in Table 1. As can be seen, the E_g values of single AgBr and NaTaO_3 are 2.59 and 3.77 eV,

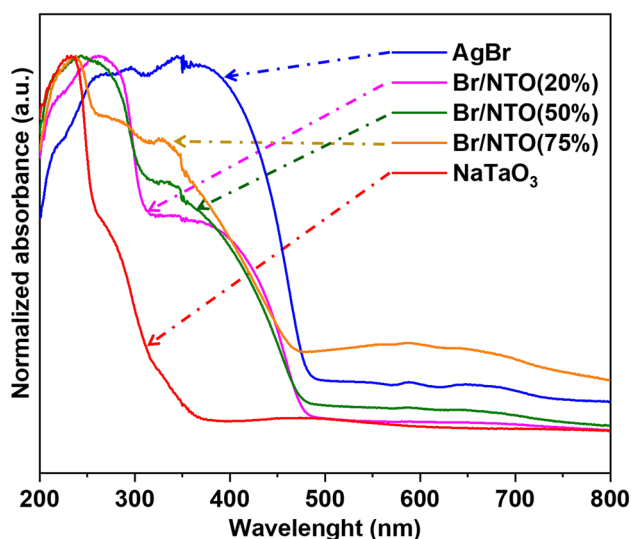


Fig. 3 UV–Vis diffuse reflectance spectra of the indicated samples

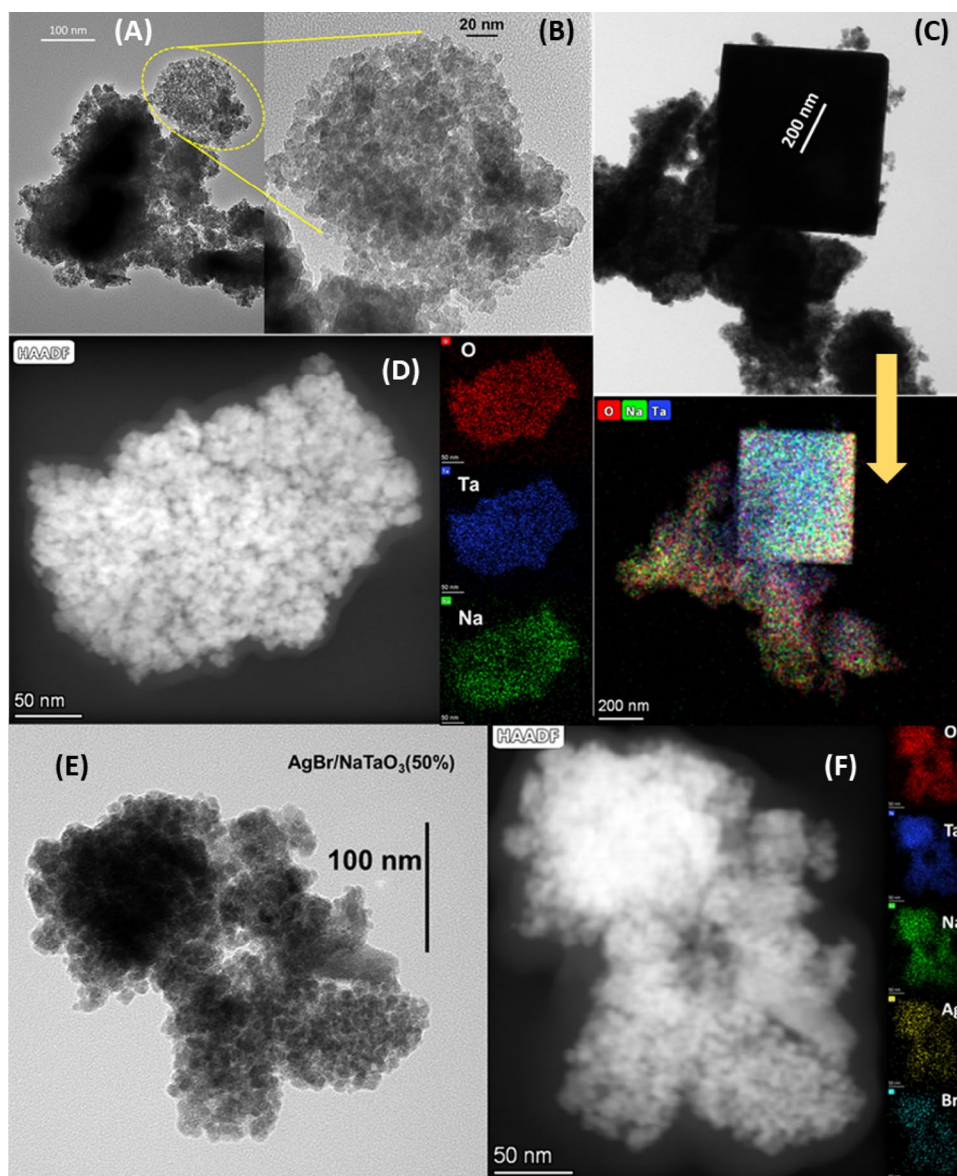
respectively; and the E_g values of AgBr/ NaTaO_3 coupled samples are close and lower than the band gap value for AgBr sample. This indicates that AgBr/ NaTaO_3 composites, compared to single AgBr and NaTaO_3 catalysts, have the ability to produce more photoexcited electron–hole pairs, increasing its photocatalytic capacity [24, 25].

The morphology of the samples has been studied by TEM and selected aspects of the TEM analysis of the indicated samples are shown in Fig. 4. The Br/NTO(50%) sample has been selected as representative of the composites. As can be seen, the synthesized NaTaO_3 has a morphology consisting of very small (20–10 nm) interconnected nano-sheets with irregular edges and a high degree of agglomeration (Fig. 4A and magnified detail in Fig. 4B). However, next to these small particles, a small number of large square particles were observed, with a size of about 400 nm (Fig. 4C) and with the same homogeneous distribution of Na, Ta and O elements. According to the elemental mapping, the Na, Ta and O atoms are homogeneously distributed both in the nanosheets and in the square particles. These square particles are not a surprise, because in several works reporting the synthesis of NaTaO_3 by hydrothermal method, particles with cuboid form was obtained [26–30]. In the case of Br/NTO(50%), the particles are very similar to the nano-sheets observed for NaTaO_3 , with the same interconnections and size. The elemental mapping shows that Na, Ta and Ag atoms are homogeneously distributed, so this confirm that the AgBr/ NaTaO_3 composite is formed (Fig. 4F).

In general, the particle size of a powder sample can be obtained by direct methods (e.g., TEM) or indirect methods (e.g., X-ray diffraction). The size determined by the different methods does not necessarily coincide. In fact, the estimated values are often different in each case. Thus, with TEM, direct images of the particles are obtained and the individual size can be determined (if there is no severe aggregation) and thus a size distribution in the powder sample can be obtained. However, the particle size cannot be determined directly by powder diffraction; in this case, the particle is divided into one or more chemically similar crystallites, which may have one or more domains originating from different causes. Furthermore, particle size determination by fitting X-ray diffractogram is only an approximation and provides an average of the crystallite sizes (apparent size). It should be remembered that the values obtained by application of the Scherrer equation (to XRD data) are very approximate, and may differ from those obtained by other techniques, such as electron microscopy, for various reasons (for example, a crystal aggregate, an intergrowth or a crystallographic macles could be seen as a single “particle” in the other techniques, but as individual crystals in diffraction).

Having said this, and related to the discrepancy between the particle (crystallite) size obtained by Sherrer formula and those observed by TEM, it should be noted that in Fig. 4,

Fig. 4 Selected TEM images of the samples NaTaO₃ (A, B, C, D) and Br/NTO(50%) (E, F). In figures (D) and (F) is present the elemental mapping for the indicated samples, with colors red, blue, green, yellow, and light blue, for the elements O, Ta, Na, Ag and Br respectively



images (A), (B), (C) and (D) correspond to different images (zones) of the pristine NaTaO₃ sample, while (D) and (F) refer to the AgBr/NaTaO₃(50%) composite. It can be seen in the image (C) that for the NaTaO₃ sample, aggregates of small particles (ranging 20–10 nm) coexist with platelets of appreciable dimensions (around 400 nm), which would contribute to the high average particle size obtained by XRD using Scherrer equation (Table 1).

Figure 5 shows the XPS results for Br/NTO(75%) (as representative of the sample). In general spectra, in addition to the C 1s peaks for adventitious carbon, peaks of Ag, Br, Na, Ta and O were observed for Br/NTO(75%) sample (Fig. 5A). The two peaks located at 367.6 ± 0.1 and 373.6 ± 0.1 eV (Fig. 5B) corresponded to Ag 3d_{5/2} and Ag 3d_{3/2} of Ag⁺ in AgBr respectively [31]. The doublet peaks observed at 182.2 ± 0.1 and 188.8 ± 0.1 eV (Fig. 5C) in the

Br 3p XPS spectrum were assigned to Br 3p_{3/2} and Br 3p_{1/2} respectively [32]. In Fig. 5D, a strong peak is observed at a binding energy of 1069.3 ± 0.1 eV, corresponding to the Na 1s in NaTaO₃ [28]. The deconvolution of Ta 4f generates two peaks at 26.5 ± 0.1 and 28.3 ± 0.1 eV (Fig. 5E), corresponds to Ta 4f_{7/2} and Ta 4f_{5/2} respectively [33]. Finally, two peaks in the O 1s region are observed at binding energies of 529.3 ± 0.1 and 530.6 ± 0.1 eV (Fig. 5F), ascribed to bulk oxygen and surface –OH groups, respectively [12, 34].

According to all characterization results, it can be confirmed that the formation of the AgBr/NaTaO₃ composites has been achieved, being particles with different sizes and morphologies. As the amount of NaTaO₃ in the composite increases, its surface area and adsorption capacity increase. Single AgBr and composite Br/

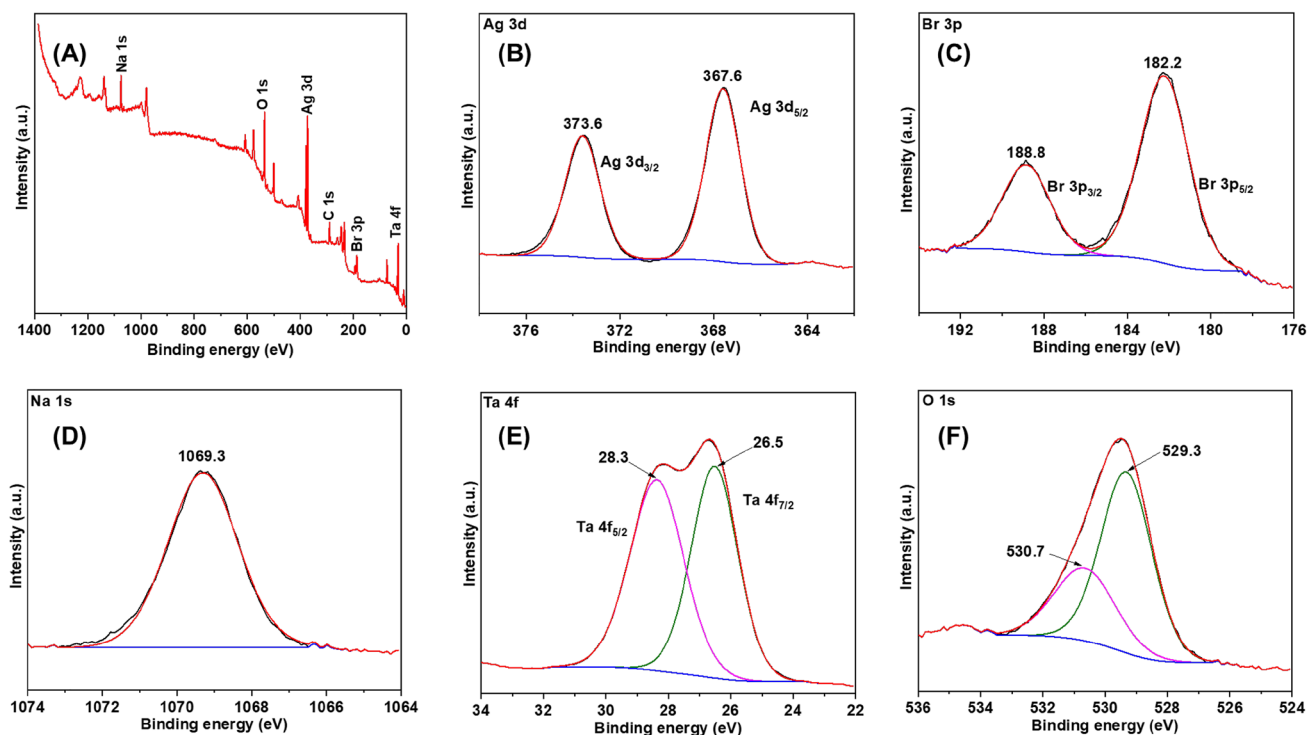


Fig. 5 XPS survey spectrum of Br/NTO(75%), as a representative sample, and high-resolution spectra showing the Ag 3d, Br 3p, Na 1s, Ta 4f and O 1s peaks profiles

NTO(X%) materials have the ability to absorb light in the visible region, while NaTaO₃ is only photoactive under UV irradiation.

3.2 Photocatalytic properties of the synthesized samples

The photocatalytic activity of all synthesized samples was carried out studying the photodegradations of aqueous solutions of two dyes (RhB and MO) and a non-dye substrate (CAFA), under two illumination conditions, UV and visible. The results are compiled in Fig. 6. In all the experiments, the photo-catalyst and the substrate were agitated for 20 min in the dark to reach the adsorption–desorption equilibrium.

Figure 6A and B shows the RhB degradation profiles under UV and visible light, respectively. In both cases, the conversion of RhB was found to be higher using the coupled materials than single catalysts separately. In the case of the NaTaO₃ catalyst, a low RhB degradation is observed under UV illumination (~25% conversion in 2 h) and practically null under visible illumination. In agreement with the E_g obtained for NaTaO₃, it is confirmed that this catalyst is only photoactive under UV light. After 5 min of illumination (UV or visible) on AgBr photo-catalyst, a small decrease in the percentage of RhB conversion is observed. This could indicate that in the first minutes of illumination,

some RhB molecules weakly adsorbed on the AgBr surface are desorbed, returning to the aqueous solution. For the coupled materials, the Br/NTO(20%) sample showed a slightly higher RhB conversion than that obtained with single AgBr, in both illumination conditions. On the other hand, Br/NTO(50%) and Br/NTO(75%) composites achieve a considerable photo-degradation of RhB, with similar conversion profiles and reaching percentages greater than 90% degradation under UV illumination.

In the case of MO photo-degradation (presented in Fig. 6C and D), it is observed that AgBr, Br/NTO(50%) and Br/NTO(75%) photo-catalysts achieve a fast degradation of MO, reaching more than 80% conversion under 10 min of UV illumination or 30 min of visible light. Furthermore, these three photo-catalysts have considerable MO adsorption capacity, following the order AgBr–CTAB > Br/NTO(50%) > Br/NTO(75%). Taking account this order, and also observing that NaTaO₃ does not adsorb any amount of MO, it could be pointed out that, as the amount of NaTaO₃ in the composite increases, its MO adsorption capacity decreases. However, it can be seen that the Br/NTO(20%) sample does not follow the indicated order and even has a higher adsorption capacity than simple AgBr. Moreover, although this sample achieves almost 100% conversion of MO in 10 min of illumination (UV or visible), as time progresses, the percentage conversion begins to decrease,

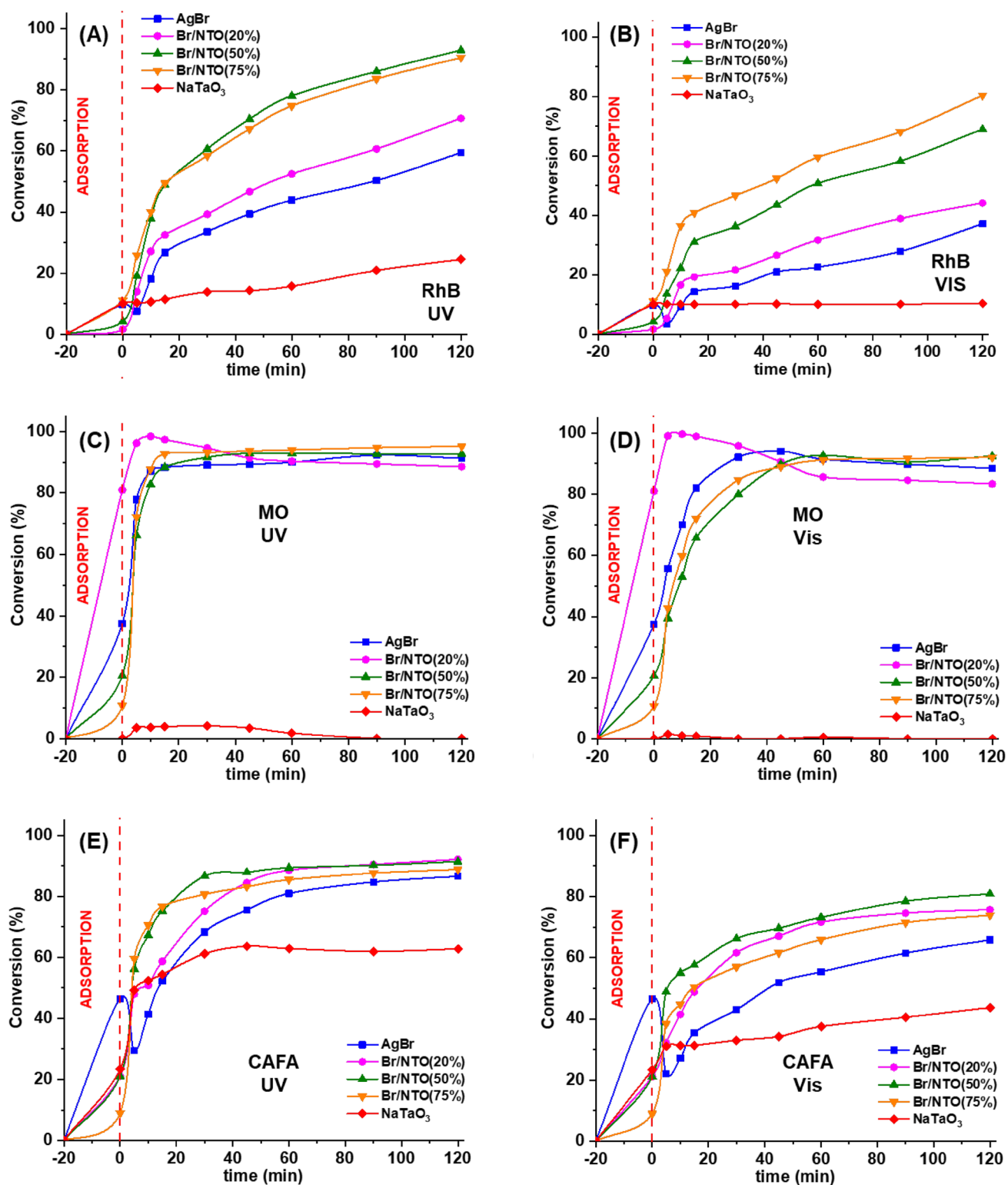


Fig. 6 Conversion plots for photocatalytic transformation of rhodamine B (RhB), methyl orange (MO) and caffeic acid (CAFA) using the indicated samples, under UV (A, C, E) and visible (B, D, F) illumination

indicating that the MO molecules begin to desorb. As mentioned above, Tang et al., synthesized AgBr by a similar procedure (using CTAB as Br source) and studied the selective adsorption of AgBr on some dyes [17]. In that work, it was determined that an AgBr complexed with CTAB showed excellent adsorption capacity for anionic dyes (such as MO) and low adsorption capacity for cationic dyes (such as RhB), because the zeta potential of AgBr (complexed with CTAB) is positive over a wide pH range. Therefore, if the AgBr surface is positively charged, the interaction between the catalyst and the anionic dye will be strengthened, resulting in an improvement in adsorption capacity. This would explain why AgBr has a high adsorption capacity on MO. In another work, Liu et al. [35] also synthesized AgBr using CTAB as a Br source, although in this case, the resulting powder was calcined in air at 400 °C for 2 h to obtain a CTAB-free AgBr. When this CTAB-free AgBr was used to photodegrade MO, no adsorption of MO on the photo-catalyst was observed. According to this, the MO adsorption capacity of our AgBr photo-catalyst could be attributed to the presence of a remaining amount of CTAB on the AgBr surface. To verify whether CTAB is present on the AgBr surface and in the coupled samples, FT-IR analysis of AgBr, NaTaO₃, Br/NTO(20%) and the CTAB precursor used in the AgBr synthesis was performed. The FT-IR results are shown in Fig. 7. As can be seen, NaTaO₃ has a broad band between 500 cm⁻¹ and 800 cm⁻¹, attributed to Ta–O stretching and Ta–O–Ta bridging stretching mode [30, 36]. For CTAB, the peak at 2916 cm⁻¹ and 2848 cm⁻¹ corresponds to asymmetric and symmetric vibrations of –(CH₂)– respectively, while the peaks at 1472 cm⁻¹ and 1383 cm⁻¹ are attributed to asymmetric and symmetric –C–H vibrations of the quaternary ammonium moiety, respectively [17, 37, 38]. When analyzing the spectra of AgBr and Br/NTO(20%), it can be seen that both have the same peaks indicated for CTAB, which confirms that both materials have an undetermined amount of CTAB on their surface. Furthermore, in Br/NTO(20%) spectra, it is possible to observe the same broad band between 500 cm⁻¹ and 800 cm⁻¹ indicated in NaTaO₃ spectra (confirming the presence of NaTaO₃ in the coupled sample), and the absence of the peak at 1383 cm⁻¹, suggesting that, the presence of NaTaO₃ in the AgBr/NaTaO₃ samples might have some influence in the (CH₃)₃N⁺ vibrations of the CTAB present in AgBr [17]. Finally, in all the spectra, it is possible to observe a wide band between 3400 and 3500 cm⁻¹ and a narrow band at 1640 cm⁻¹, related to stretching and bending vibrations of O–H from absorbed water molecules on the surface of the samples [34].

From this FT-IR analysis, it was possible to establish that, despite repeated washing of the samples, a certain amount of CTAB is retained on the surfaces of both the AgBr and the AgBr/NaTaO₃ composites. According to the reference [37], when the molar ratio of CTAB to silver nitrate is lower than

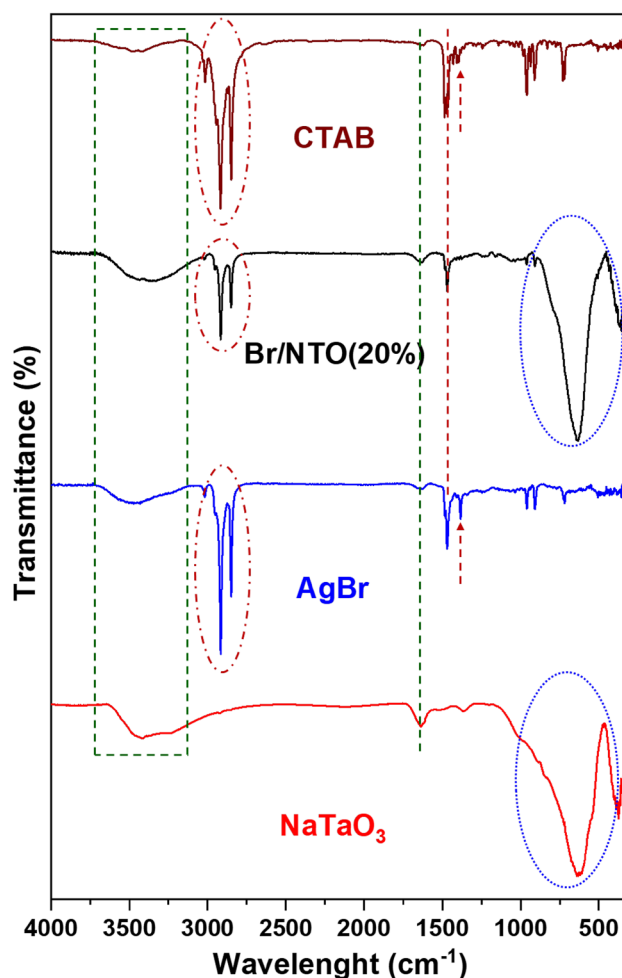
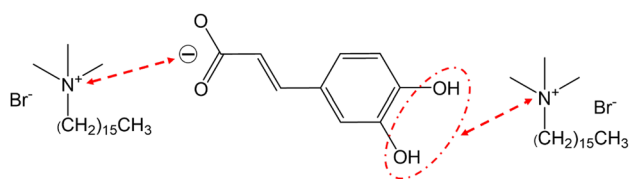


Fig. 7 FT-IR spectra of the indicated samples

1.5/1, the product would be a light yellow color, correspond to silver bromide crystal, free of CTAB. In our case, the CTAB/AgNO₃ molar ratio was always 1.18/1, obtaining a pale yellow material. Comparing the synthesis procedures of this work with the mentioned reference, we can observe that there is a difference in the initial concentrations of the aqueous solutions of CTAB and AgNO₃ used to prepare AgBr. In this way, we can assume that, for the synthesis of AgBr through aqueous solutions of AgNO₃ and CTAB, it is not only important to control the molar ratio CTAB/AgNO₃, but also the concentration of the aqueous solutions of AgNO₃ and CTAB.

Figure 6E and F shows the CAFA degradation profiles under UV and visible light, respectively. Under both illumination conditions, the conversion of CAFA is higher with the coupled AgBr/NaTaO₃(X%) materials than with the individual catalysts separately. In the case of single AgBr, a higher adsorption capacity of CAFA is observed, and this could be possible for two reasons: (i) the specific interactions between Ag⁺ ions and carboxyl group of CAFA, as we



Scheme 1 Illustrative representation of possible donor–acceptor interaction between caffeic acid molecules and quaternary ammonium cation of CTAB

suggest in a previous work [19]; (ii) a probable donor–acceptor interactions between the quaternary ammonium cation (of the remaining CTAB in AgBr surface) and the hydroxyl and carboxyl groups of CAFA, as illustrated in Scheme 1 [39]. Furthermore, it can be observed that, in the case of the AgBr–CTAB photo-catalyst, there is a decrease in the CAFA conversion rate in the first 5 min of illumination (UV or visible), and after that time, the conversion rate starts to increase. This indicates that, during the first few minutes, the incident light (UV or visible) causes a photochemical desorption of some CAFA molecules from the AgBr surface. In the case of single NaTaO₃, a considerable adsorption capacity of CAFA is observed. This suggests that there could be some interaction between the hydroxyl and/or carboxyl groups of CAFA and the sodium and tantalum cations (Na⁺ and Ta⁵⁺) on the NaTaO₃ surface. Nevertheless, despite the initial adsorption, the final conversion percentages achieved using NaTaO₃ are lower compared to those obtained using the AgBr and Br/NTO(X%) samples, in both illumination conditions (Fig. 6E and F). An additional information that is important to mention is that there is a different behavior between UV and visible light performance for CAFA degradation using NaTaO₃ as photocatalyst. Figure 8 shows the evolution of the UV and visible absorption spectra during

the photocatalytic degradation of CAFA using NaTaO₃ as photocatalyst, under UV (Fig. 8A) and visible (Fig. 8B) illumination. Under visible light, it can be noted that, after the adsorption process in dark, a slow decrease of the maximum peak at 312 nm occurs, without the appearance of additional bands in the spectra. On the contrary, under UV illumination conditions, it is observed that after the adsorption process in the dark, in the first five minutes under UV light there is a rapid decrease of the maximum peak at 312 nm, and from then on, this decrease is slower. In addition, the simultaneous appearance of an absorption band between 360 and 400 nm is observed, which increases during the first 45 min of UV illumination and decreases thereafter. This kind of behavior of CAFA under UV light was observed in a previous investigation of our group [40], and can be explained on the *trans*-caffeic acid degradation model, proposed in the reference [41], which considers the following steps for the degradation mechanism of *trans*-caffeic acid: (i) the reversible *trans/cis* isomerization of caffeic acid, (ii) the generation of esculetin from *cis*-caffeic acid and (iii) the formation of vinyl catechol and protocatechuic acid, by two different pathways from *trans*-caffeic acid. A summary of these pathways of photodegradation of *trans*-caffeic acid is presented in Scheme 2. According to this mechanism, under UV irradiation, *trans/cis* isomerization of caffeic acid occurs and, from *cis* isomer, the photodegradation (in the presence of NaTaO₃) proceeds toward the formation of esculetin. In contrast, under visible irradiation, the *cis* isomer is not formed, and photo-degradation of *trans*-caffeic acid proceeds to the formation of vinyl catechol and protocatechuic acid. This would be the reason why the absorption band between 360 and 400 nm is observed only under UV light.

As shown in Table 3 (see below), most of the studies related to systems similar the one in the present study have used RhB as a substrate for photocatalytic degradation. We

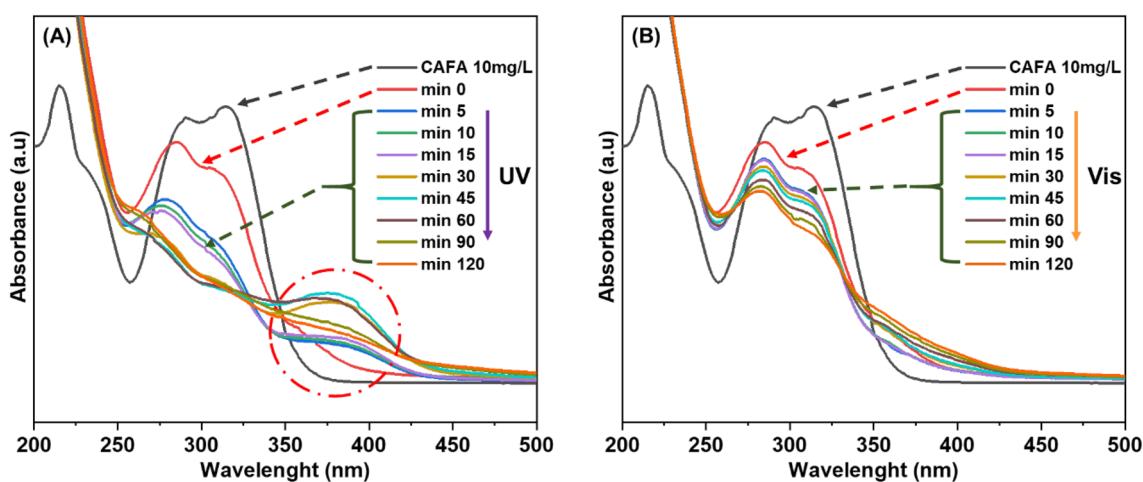
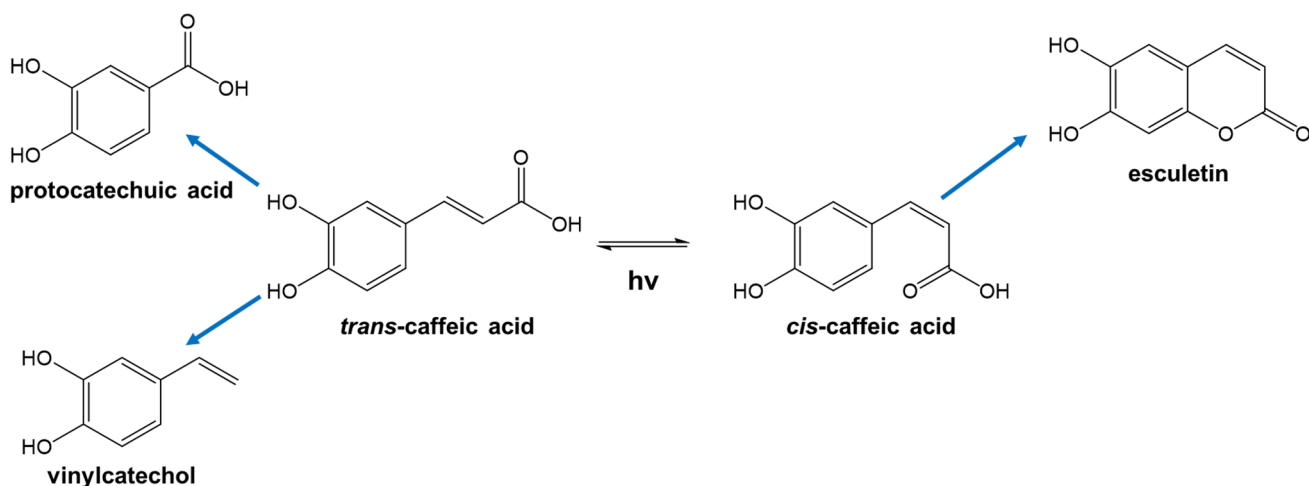


Fig. 8 UV–visible spectra obtained for various UV and visible illumination times of caffeic acid (10 ppm) in the presence of NaTaO₃ catalyst



Scheme 2 Proposed mechanism for photodegradation of *trans*-caffeic acid

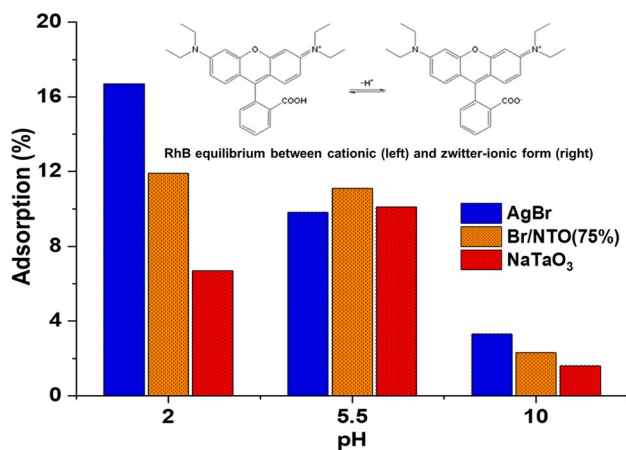


Fig. 9 The effect of pH on the adsorption capacity of AgBr, AgBr/NaTaO₃(75%) and NaTaO₃ catalysts toward RhB

have indicated that the interfacial interaction between RhB, MO and CA with the particles determines the observed difference in photo-catalysis, suggesting that surface charge is a key factor as often invoked in these processes in the literature. To further investigate this question, we conducted a series of experiments on the adsorption capacity and photocatalytic conversion percentages of RhB at different pH values. The initial concentrations of RhB were 10 ppm (10 mg/L) with a catalyst dose of 1 g/L in 100 mL volume, for all experiments performed. Prior to the light-driven photocatalytic degradation process, the suspensions were kept in the dark under continuous magnetic stirring for 20 min to evaluate the adsorption capacity of the samples at different pH values. Magnetic stirring and continuous air bubbling were applied to provide a uniform suspension of the photocatalyst in solution.

Figure 9 shows the results of the adsorption percentages of RhB under the experimental conditions referred to. It can be seen that the two single components of the AgBr–NaTaO₃ composite sample display adsorption capacity toward RhB when tested as individual samples. However, it is interesting to note that the adsorption capacity of RhB is sensitive to the indicated pH values. Therefore, if the AgBr surface is positively charged, the interaction between the catalyst and the cationic dye (RhB) will be diminished, resulting in a reduction of the adsorption capacity. Surprisingly, this is not what the graphs in Fig. 9 show. Thus, assuming the result of Tang et al. [17] that zeta potential of AgBr–CTAB is positive over a wide pH range, although it decreases as the pH value increases, one would expect a low adsorption capacity of RhB at pH = 2 given its cationic character, but the opposite is observed. A plausible explanation for these results could be related to the way in which RhB adsorbs on the AgBr surface. Thus, given the structural characteristics of RhB, the adsorption results of RhB with the AgBr catalyst should not be associated with interactions of its cationic parts with the surface of the material but rather with a possible donor interaction of the rings of the molecule with the positively charged surface of the catalyst in a planar situation. Assuming this consideration, it is to be expected that at higher pH values the adsorption capacity would be reduced since the surface of the catalyst would be less positive under these conditions.

If we observe the conversion percentages of RhB at different pH values using the AgBr/NaTaO₃(75%) composite (Table 2), we can see variations in the conversion rates of RhB but cannot be rationalized according to a single factor, given that the pH of the reaction medium determines the surface charge, the way in which the molecule (depending on its structure) is coupled to the surface centers, the photo-sensitizing characteristics of the dye, etc. In any case,

Table 2 Conversion percentages (%) of photocatalytic degradation of RhB at different pH conditions using AgBr/NaTaO₃(75%) as photocatalyst, under UV and visible illumination

pH	UV		Visible	
	60 min	120 min	60 min	120 min
2	77.5	91.7	40.6	58.3
5.5	74.7	90.5	59.5	80.3
10	62.2	77.8	39.9	58.5

it seems that the adsorption capacity of Br/NTO(75%) at pH = 5.5 is optimal to obtain acceptably good degradation values of RhB both in the UV and in the visible.

In the case of NaTaO₃, the adsorption of RhB change with pH value, and this could be explained from the point zero charge (PZC) of NaTaO₃ and the different forms of RhB in aqueous solutions. For low concentrations solutions, RhB has different molecular forms, which depend on the pH solution, changing between cationic RhB (acidic conditions) to zwitterionic RhB (basic conditions) (scheme inserted in Fig. 9) [42, 43]. Moreover, according to Qian Cheng et al. [44], the PZC of NaTaO₃ (synthesized hydrothermally) is 3.5. Thus, at pH = 2 the NaTaO₃ surface is positive charge and has a low adsorption of RhB because the molecule is in the cationic form. At pH = 5.5 the RhB equilibrium still has a higher concentration of cationic form, but now the NaTaO₃ surface is negative charge, so this could explain the highest adsorption at this pH. At pH = 10 the NaTaO₃ surface is negative charge and RhB is in the zwitterionic conformation, conditions that respond to low adsorption at this value of pH.

Finally, the adsorption of RhB in the surface of Br/NTO(75%) would result from a combination of the phenomena that occur on the AgBr and NaTaO₃ surfaces at different pH values, as shown in Fig. 9.

Reusability tests are an important part of studies of photocatalysts for practical applications. For this purpose, we have evaluated the photocatalytic activity of the Br/NTO(75%) sample in the photocatalytic degradation of RhB in five successive reuse cycles. The experiments were carried out using the same reaction conditions as previously indicated for the photocatalytic activity test. After 2 h of illumination (UV or visible), the photocatalyst was recovered from the reaction mixture by filtration, rinsed with deionised water and subsequently reused in the next cycle. The results of percentage conversion of RhB for every cycle are present in Fig. 10. As can be seen, under both lighting conditions, high conversion percentages are obtained in the first cycle, but there is a considerable decrease in the conversion percentage thereafter. Under UV illumination (Fig. 10A), this decrease continues until the fourth cycle and then the percentage conversion remains constant. Under visible illumination (Fig. 10B), the conversion percentages are practically constant between the

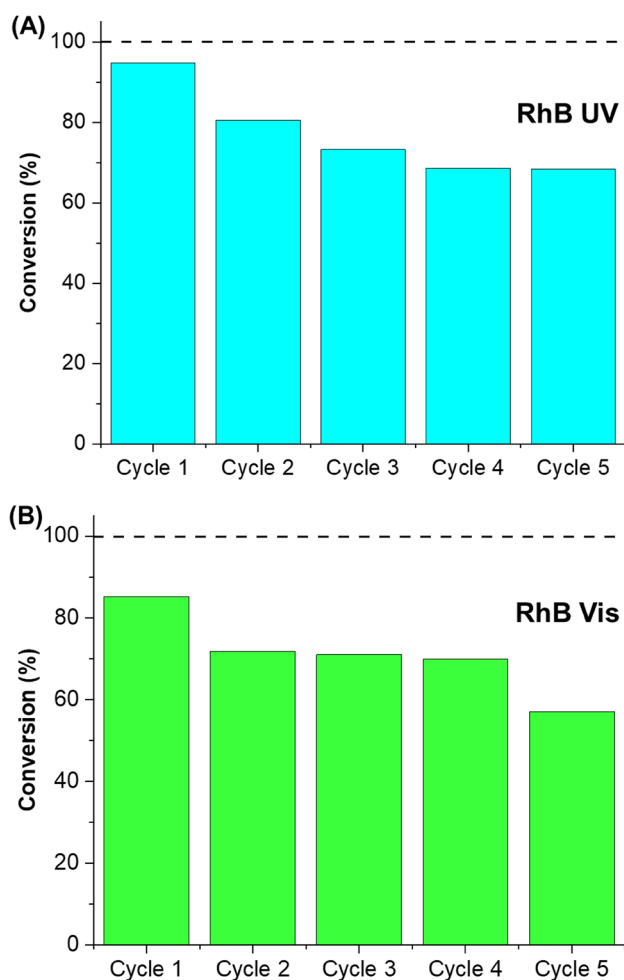


Fig. 10 Consecutive cycling runs in the photocatalytic degradation of RhB using the Br/NTO(75%) catalyst, under UV (A) and visible illumination (B)

second and fourth cycles, since in the fifth cycle the conversion percentage drops considerably again.

To investigate possible causes for the loss of activity observed during reuse, the following experiments have been carried out. The Br/NTO(75%) sample used in the successive cycles of UV photocatalytic degradation of RhB, once dried, was studied by XRD and XPS, and the results were compared with those obtained for the sample before its use as a photocatalyst; these comparative results are shown in Figs. 11 and 12.

The XRD pattern of Br/NTO(75%) composite (Fig. 11A), it is similar to the patterns obtained with the other coupled samples, where the peaks correspond to the monoclinic NaTaO₃ and cubic AgBr phases. However, after the successive cycles of UV photocatalytic degradation of RhB (Fig. 11B), the XRD pattern of Br/NTO(75%) presented two new peaks (indicated with orange triangles), that correspond to cubic phase of metallic silver (JCPDS

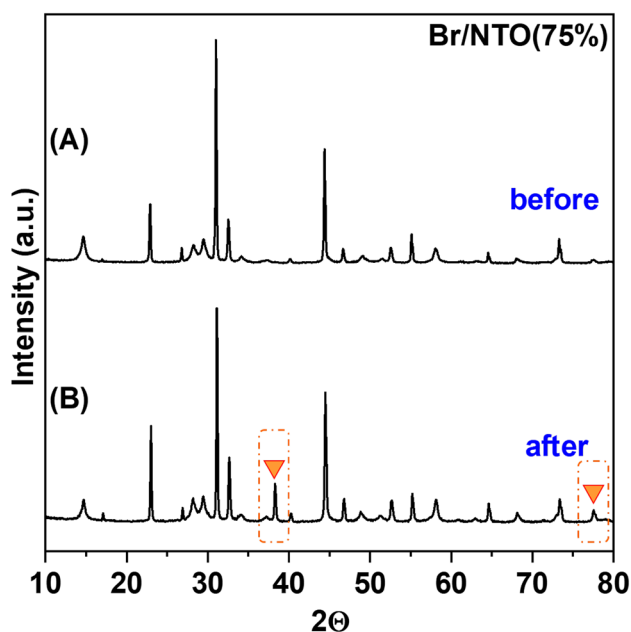


Fig. 11 XRD patterns of Br/NTO(75%) sample before (A) and after (B) of the successive cycles of photocatalytic degradation of RhB

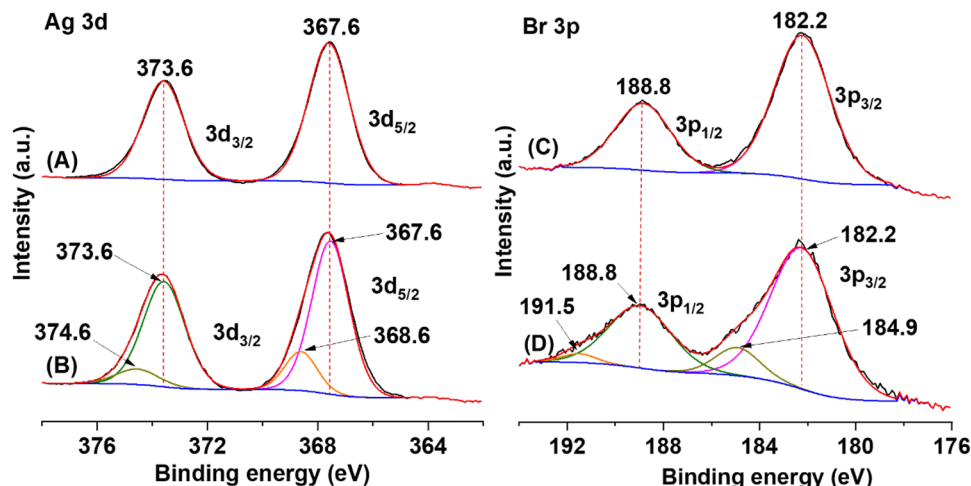
01–087–0718). The remaining peaks corresponding to metallic silver are overlapped with the peaks belonging to cubic AgBr. These results are agree with the change of color of the composite after being illuminated with UV light, changing from pale yellow to gray–black color.

Figure 12 shows the Ag 3d and Br 3p regions of the coupled Br/NTO(75%) before (Fig. 12A and C) and after (Fig. 12B and D) being used in the successive cycles of UV- photocatalytic degradation of RhB. As previously stated in the high-resolution XPS spectra of Br/NTO(75%) sample, the peaks at 367.6 ± 0.1 eV and 373.6 ± 0.1 eV, correspond to Ag $3d_{5/2}$ and Ag $3d_{3/2}$ of Ag^+ in AgBr respectively (Fig. 12A), and the peaks at 182.2 ± 0.1 eV and 188.8 ± 0.1 eV, assigned to Br $3p_{3/2}$ and Br $3p_{1/2}$ of Br^- in

AgBr respectively (Fig. 12C). After the successive cycles of UV photocatalytic degradation of RhB, noticeable differences are observed in the XPS profiles of Ag 3d and Br 3p of the sample used. In the case of Ag 3d region, the two peaks can be divided in two components. The peak for Ag $3d_{5/2}$ is divided in two peaks at 367.6 ± 0.1 eV and 368.6 ± 0.1 eV, and the peak for Ag $3d_{3/2}$ is divided in two peaks at 373.6 ± 0.1 eV and 374.6 ± 0.1 eV. According to the above assignment, the peaks at 367.6 and 373.6 should be assigned to Ag^+ of AgBr in Br/NTO(75%). Due to the closeness of the binding energy values of the silver species, it is difficult to assign the oxidation states of silver. However, the shift of the Ag 3d peaks toward higher values of binding energies and the decrease in the intensities of the Ag^+ peaks of AgBr, are signs of the formation of Ag^0 [45, 46]. Thus, the two peaks at 368.6 ± 0.1 eV and 374.6 ± 0.1 eV (Fig. 12B) are assigned to Ag^0 in the surface of Br/NTO(75%) sample after successive cycles of UV photocatalytic degradation of RhB, and this assignment is in agreement with the metallic silver present in the XRD pattern of this material after use under UV light (Fig. 11B). In the case of Br 3p region, the two peaks can be divided in two components. The peak for Br $3p_{3/2}$ is divided in two peaks at 182.2 ± 0.1 eV and 184.9 ± 0.1 eV, and the peak for Br $3p_{1/2}$ is divided in two peaks at 188.8 ± 0.1 eV and 191.5 ± 0.1 eV (Fig. 11D). According to the above assignment, the Br 3p peaks at 182.2 and 188.8 should be assigned to Br^- of AgBr in Br/NTO(75%). The two peaks at 184.9 ± 0.1 eV and 191.5 ± 0.1 eV can be assigned to Br species on the surface of Br/NTO(75%) composite, probably interacting with Ta^{5+} ions on the catalyst surface.

To further investigate the changes of the AgBr coupled to the AgBr/NaTaO₃(75%) sample during the reuse cycles, the amounts of silver and bromide released into the reaction medium after prolonged UV illumination (2 h under UV illumination) have been evaluated. While the amount of Ag found in the medium (with respect to the de-ionized water

Fig. 12 XPS analysis of Ag 3d and Br 3p regions on the surface of Br/NTO(75%) sample before (A, C) and after (B, D) of the successive cycles of photocatalytic degradation of RhB



blank) is less than 0.001 mg/L, the amount of bromide is 16.2 mg/L. Taking into account the concentration of catalyst used (0.1 g in 100 mL) and the molar percentage of AgBr in the sample tested (AgBr/NaTaO₃(75%)), a simple calculation indicates that 2.02×10^{-5} mol of bromide are released into the medium, which represents a loss (in molar percentage) of approximately 7.62 mol % after 2 h of UV illumination. However, it should be noted that as a certain amount of the CTAB is retained in the sample, part of the amount of bromide released to the medium could come from the CTAB in the sample itself. In any case, this result not only agrees with the observations obtained by XPS and XRD, but also indicates that AgBr coupled to NaTaO₃ is stable, transforming Ag⁺ to Ag⁰ and retaining much of the bromide in the sample (possibly bound to the Ta⁵⁺ cations on the surface).

In accordance with above mentioned, it can be assumed that the change in color of the coupled material Br/NTO(75%), during the photocatalytic degradation of RhB, corresponds to a change in the characteristics of the catalyst toward a system with a composition different from the initial one. The adsorbed Br species could cover and reduce the reaction sites on the surface of the coupled material, and this could be the reason for the decrease in his photocatalytic activity during the successive cycles in the photodegradation of RhB. With these results, it can be mentioned that Br/NTO(75%) does not have a rentable reusability, at least for RhB degradation.

3.3 Proposed features for a tentative mechanism

In the previous section, it has been determined that the photocatalytic activity of the AgBr/NaTaO₃ composites not only depends on the type of substrate to be degraded, but also on the type of incident light, UV or visible. However, knowing the positions of the conduction and valence bands of each photocatalyst allows us to identify, among other things, the migration of photogenerated charge carriers and the type of heterojunction formed. The conduction band edge (CB) and valence band edge (VB) positions of the synthesized parent samples, AgBr and NaTaO₃, have been estimated by the following empirical expressions [29, 47]:

$$E_{VB} = \chi - E^e + 0.5E_g.$$

$$E_{CB} = E_{VB} - E_g.$$

where E_{VB} and E_{CB} are the valence and conduction band potentials, respectively, E^e is the energy of free electrons on the hydrogen scale (about 4.5 eV vs. NHE), and χ is the electronegativity of the semiconductor, were the values for AgBr and NaTaO₃ are 4.42 eV [19] and 5.50 eV [47], respectively. According to these expressions, the E_{VB} and E_{CB} values for AgBr were calculated to be 1.21 and -1.37 eV

vs. NHE, respectively, while the E_{VB} and E_{CB} values for NaTaO₃ were 2.89 and -0.89 eV vs. NHE, respectively, as plotted in Fig. 13. Based on these results and the position of CB and VB of AgBr and NaTaO₃, the heterojunction between these two photocatalysts corresponds to a type II junction, which is the most desirable for photocatalysis [48]. The schematic illustration of Fig. 13 describes the formation of staggered gap (type II) heterojunctions at the interface of AgBr/NaTaO₃ composite. When the composite is illuminated (UV or visible light), this heterojunction facilitates the transfer of photogenerated electrons from the CB of AgBr to the CB of NaTaO₃; in the same way, the photogenerated holes in the VB of NaTaO₃ are transferred to the VB of AgBr (only under UV light). This process leads to an improvement in the spatial separation of the generated charge carriers, which increases their photocatalytic activity, in line with strategies reported in a recent review [1]. According to the results obtained in the photocatalytic activity of the coupled materials AgBr/NaTaO₃ in the degradation of RhB and caffeic acid, it can be determined that a synergistic effect is obtained in the heterojunction of both materials, which increases the photocatalytic activity of the coupled system compared to that obtained by both parent materials under the same operating conditions; this charge transfer mechanisms have been suggested for the development of photocatalysis [1].

Some radicals are obviously present in the mechanism proposed in Fig. 13, which could be involved in the photocatalytic oxidation process. The estimated VB edge of NaTaO₃ (2.89 eV) is more positive than the standard redox potential of •OH/OH⁻ (1.99 eV) [49], so the photogenerated hole (h⁺) is more oxidative than •OH radical. The standard redox potential of O₂/O₂^{•-} (-0.33 eV) [19] is

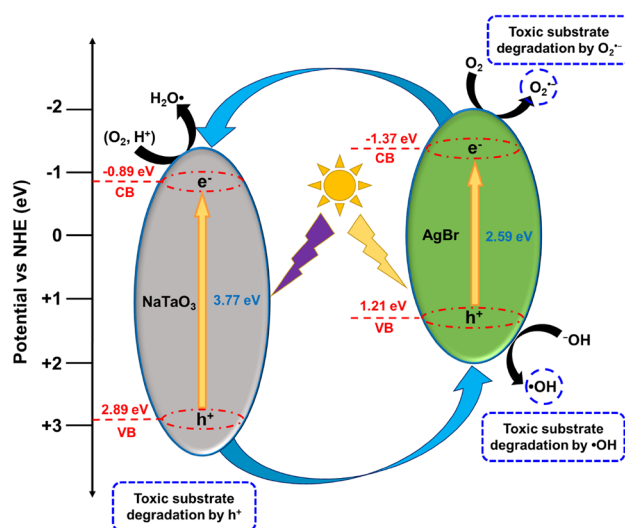


Fig. 13 Proposed schematic mechanism according to a type II junction scheme for the AgBr/NaTaO₃ composite

less negative than the CB of AgBr (− 0.89 eV) and NaTaO₃ (− 1.37 eV), which indicate that both semiconductors can reduce molecular oxygen. Nevertheless, depending on the acidic or basic conditions of the medium, the properties of O₂^{•−} are different, because at pH close to 4.8, the addition of a proton to O₂^{•−} occurs. [50]. Since the solutions used in our experiments have pH close to 5 and according to the standard redox potential of {O₂, H⁺/•O₂H} (− 0.046 eV) [50], it is possible that O₂ can be reduced to •O₂H in the CB of the two photocatalysts during the electron transfer.

Additionally, the dye sensitization plays an important role in the photocatalytic degradation of RhB and MO. The lowest unoccupied molecular orbital (LUMO) and the highest occupied molecular orbital (HOMO) are − 1.0 and 1.1 eV vs. NHE for RhB [51] and − 1.87 and 0.14 eV vs. NHE for MO [52]. For RhB and MO, their photo-excited electrons in the LUMO of these dyes can be transferred to the conduction band of NaTaO₃ catalyst, because the LUMO of RhB and MO (− 1.0 and − 1.87 eV vs. NHE respectively) are highest than the conduction band of NaTaO₃ (− 0.89 eV vs. NHE). In addition, the LUMO of MO is even highest than conduction band of AgBr (− 1.37 eV vs. NHE), so the photo-excited electrons in MO can be transferred to the conduction band of NaTaO₃ or AgBr. In summary, the suitable band alignment of the LUMO–HOMO of the dyes and the bands edges of the catalysts, enhanced the photo-energy conversion efficiency observed for RhB and MO degradation.

As stated in the introduction to this work, the construction of heterojunctions by coupling two semiconductors has proven to be one of the most efficient ways to realize the spatial separation of photoexcited electron–hole pairs; the coupling between AgBr and NaTaO₃ is within the context of that goal. If the two semiconductors possess different Fermi energy (E_F) levels or work functions, an integrated electric field is expected to form at the heterojunction interface due to the spontaneous diffusion of electrons from the semiconductor with the higher E_F to the one with the lower E_F. It should be noted that the formation of the integrated electric field at the heterojunction interface and the operation of photoexcited carrier transfer depend on many factors, such as the semiconductor (p-type or n-type), the Fermi level (or work function), conduction band/valence band potentials of the semiconductors, etc.; so positioning the band alignment in the AgBr/NaTaO₃ heterojunction and setting the LUMO/HOMO values (of each organic) there would be complex but rigorously correct. In truth, in the schematic presented in Fig. 13, the energies represented are those estimated without contact between the semiconductors and this is a simplification of the system given that upon contact between the two semiconductors, the energy levels would be drastically readjusted, and band bending would occur. However, regardless of whether we agree with the above observation, we maintain the way of presenting the diagram as shown in

Fig. 13, mainly because in the scientific literature diagrams are described in the way we present the diagram here, being qualitatively valid for a tentative proposal of the mechanism, as we have used in other previously published works [19, 34] and other authors also present it in this way [12, 14–16, 24, 31, 35, 45, 47].

Before concluding this work, it is convenient to compare our results with those obtained by other authors using other similar materials. Table 3 presents a summary of some works in which materials like those synthesized in this work have been tested for the study of the degradation of the organic pollutants indicated and the operating conditions of each investigation. From the results referenced in this table, it can be seen that, in almost all the works mentioned, a single substrate was used to evaluate the photocatalytic activity of the materials, with the RhB dye being the most commonly used, which also has a photo-sensitizing effect, which could not have been considered. In our work, we have used two dyes, RhB and MO, and this has shown that our catalysts have a higher affinity for anionic dyes (such as MO), due to the CTAB molecules on the surface of the material. For this reason, the AgBr/NaTaO₃(50%) coupled material achieves a higher adsorption and degradation of MO compared to RhB. In addition, the photo-activity on a colorless substrate (CAFA) was also evaluated, obtaining high degradation percentages under both UV and visible light. In summary, it can be concluded that the synthesized AgBr/NaTaO₃(50%) photo-catalyst has a considerable RhB degradation under UV illumination, and an excellent catalytic performance for MO and CAFA degradation in both UV and visible illumination conditions. Regardless of this, we think that our work brings new insights to the study of the NaTaO₃ system coupled with AgBr.

4 Conclusion

NaTaO₃ was synthesized hydrothermally and then coupled with AgBr at different molar ratios by in situ AgBr deposition on water suspension of NaTaO₃. From the characterization results, we obtained a successful coupling between AgBr and NaTaO₃, and the AgBr/NaTaO₃ composites are particles with different sizes and morphologies. NaTaO₃ is only photoactive under UV irradiation, while the coupled samples and single AgBr can absorb visible light; in addition, these samples have an undetermined quantity of CTAB on their surfaces, from the remaining CTAB used as a source of Br in the synthesis of AgBr.

Singles and coupled samples were used for photodegradation three different toxic substrate: rhodamine B (RhB), methyl orange (MO) and caffeic acid (CAFA) under two illumination conditions (UV and visible light). Compared to single AgBr and NaTaO₃ photocatalysts, AgBr/NaTaO₃

Table 3 Comparison of the photocatalytic performance of as-prepared photocatalyst with other reported photocatalysts

Photocatalyst	Light source	Targer pollutant	Conc. (mg/L)	Volumen (mL)	Mass composite (mg)	Degradation (%)	Time (min)	References
(30 wt%)Ag ₃ PO ₄ /NaTaO ₃	Visible	RhB	10	100	100	97	25	[53]
(7:3 wt. ratio)Ag ₂ O/NaTaO ₃	Visible	RhB	10	100	50	89.6	100	[29]
(50 wt%)CuBi ₂ O ₄ /NaTaO ₃	Visible	MB	20	60	100	96	100	[47]
(H-3)AgCl/Ag ₂ O/NaTaO ₃	Visible	RhB	10	100	50	96	60	[33]
(20 wt%)G/g-C ₃ N ₄ /NaTaO ₃	Visible	RhB	20	80	30	100	70	[30]
(2% molar)La-NaTaO ₃	UV	ST	10	100	100	90	120	[26]
(8:1 molar ratio)CdS/NaTaO ₃	Visible	RhB	0.50	100	50	97.2	110	[54]
(s-800)S,N-NaTaO ₃	Visible	RhB	20	100	100	95	60	[55]
(0.6:1 molar ratio)Ag-NaTaO ₃	Visible	RhB	10	100	100	85	240	[56]
(70 wt%)AgBr/AgTaO ₃	Visible	MO	6.5	50	50	90	30	[46]
AgBr/NaTaO₃(50%)	UV	RhB	10	100	100	93.0	120	This study
		MO	20	100	100	92.9	45	
		CAFA	10	100	100	91.4	120	
	Visible	RhB	10	100	100	69.0	120	
		MO	20	100	100	92.6	60	
		CAFA	10	100	100	90.9	120	

Bold values indicate the numbers corresponds to % degradation achieved with RhB, MO and CAFA

RhB rhodamine B, CAFA caffeic acid, MO methyl orange, MB methylene blue, ST safranin T

composites show higher photocatalytic activity for RhB and CAFA degradation under both illumination conditions. It was observed that the adsorption capacity exhibited by AgBr/NaTaO₃ composites and single AgBr is highly dependent on the characteristics of the substrate, whether it is cationic or anionic. Thus, the interactions between the quaternary ammonium cation (of the CTAB molecules present on the surface of the AgBr/NaTaO₃ composite and plain AgBr) with the hydroxyl and carboxyl group of CAFA and the negative charge of the MO could be the reason for the enhanced adsorption capacity of these substrates, while for RhB the cationic and zwitterionic forms (sensitive to pH values) may condition its adsorption capacity and form with the NaTaO₃ surface.

The heterojunction between AgBr and NaTaO₃ corresponds to a type II junction, and the coupling of these two catalysts generates a synergistic effect that improves their photocatalytic activity, compared to that obtained by both parent materials under the same operating conditions.

The AgBr/NaTaO₃ coupled materials have proven to be possible candidates for water remediation by

heterogeneous photocatalysis under UV or visible light. Our results provide new insights for the development of visible light photocatalysts, in particularly when the wide band gap NaTaO₃ semiconductor is used.

Acknowledgements The authors thank the general research services (XPS, TEM, SEM, XRF, etc.) of the CITIUS/University of Seville (Spain). Authors are also grateful for the funding granted by the Reference Project PID2021-122413NB-I00 in the area of Environmental Sciences and Technologies in the framework of the Knowledge Generation Projects 2021 (Ministry of Science and Innovation, Spain). Felipe Puga is grateful for the funding by Scholarships Chile, from the National Agency of Research and Development of Chile (ANID, Chile).

Author contributions F. P. Conceptualization, Data curation, Investigation, Writing-original draft. J.A. N.: Supervision, Resources, Methodology, Writing-original draft. M.C.H.: Formal analysis, Supervision, Validation.

Funding Open Access funding provided thanks to the CRUE-CSIC agreement with Springer Nature.

Data availability All data generated or analyzed during this study are included in this article, in the form of figures, tables and references.

Declarations

Conflict of interest The authors declare that they have no known competing financial interests or personal relationships that could have appeared to influence the work reported in this paper.

Open Access This article is licensed under a Creative Commons Attribution 4.0 International License, which permits use, sharing, adaptation, distribution and reproduction in any medium or format, as long as you give appropriate credit to the original author(s) and the source, provide a link to the Creative Commons licence, and indicate if changes were made. The images or other third party material in this article are included in the article's Creative Commons licence, unless indicated otherwise in a credit line to the material. If material is not included in the article's Creative Commons licence and your intended use is not permitted by statutory regulation or exceeds the permitted use, you will need to obtain permission directly from the copyright holder. To view a copy of this licence, visit <http://creativecommons.org/licenses/by/4.0/>.

References

- Wang, H., Li, X., Zhao, X., Li, C., Song, X., Zhang, P., & Huo, P. (2022). A review on heterogeneous photocatalysis for environmental remediation: From semiconductors to modification strategies, Chinese. *Journal of Catalysis*, *43*, 178–214.
- Youssef, Z., Colombeau, L., Yesmurzayeva, N., Baros, F., Vanderesse, R., Hamieh, T., Toufaily, J., Frochot, C., & Roques-Carnes, T. (2018). Dye-sensitized nanoparticles for heterogeneous photocatalysis: Cases studies with TiO₂, ZnO, fullerene and graphene for water purification. *Dyes and Pigments*, *159*, 49–71.
- Dong, S., Feng, J., Fan, M., Pi, Y., Hu, L., Han, X., Liu, M., Sun, J., & Sun, J. (2015). Recent developments in heterogeneous photocatalytic water treatment using visible light-responsive photocatalysts: a review. *RSC Advances*, *5*, 14610–14630.
- Reddy, P. A. K., Reddy, P. V. L., Kwon, E., Kim, K. H., Akter, T., & Kalagara, S. (2016). Recent advances in photocatalytic treatment of pollutants in aqueous media. *Environment International*, *91*, 94–103.
- Miklos, D. B., Remy, C., Jekel, M., Linden, K. G., Drewes, J. E., & Hübner, U. (2018). Evaluation of advanced oxidation processes for water and wastewater treatment – A critical review. *Water Research*, *139*, 118–131.
- Rajaiitha, P. M., Hajra, S., Sahu, M., Mistewicz, K., Toróñ, B., Abolhassani, R., Panda, S., Mishra, Y. K., & Kim, H. J. (2022). Unraveling highly efficient nanomaterial photocatalyst for pollutant removal: a comprehensive review and future progress. *Mater. Today Chem.*, *23*, 100692.
- Wei, K., Faraj, Y., Yao, G., Xie, R., & Lai, B. (2021). Strategies for improving perovskite photocatalysts reactivity for organic pollutants degradation: A review on recent progress. *Chemical Engineering Journal*, *414*, 128783.
- Wang, H., Zhang, Q., Qiu, M., & Hu, B. (2021). Synthesis and application of perovskite-based photocatalysts in environmental remediation: A review. *Journal of Molecular Liquids*, *334*, 116029.
- Mai, H., Chen, D., Tachibana, Y., Suzuki, H., Abe, R., & Caruso, R. A. (2021). Developing sustainable, high-performance perovskites in photocatalysis: Design strategies and applications. *Chemical Society Reviews*, *50*, 13692–13729.
- Sudrajat, H., Babel, S., Thushari, I., & Laohhasurayotin, K. (2019). Stability of La dopants in NaTaO₃ photocatalysts. *Journal of Alloys and Compounds*, *775*, 1277–1285.
- Grabowska, E. (2016). Selected perovskite oxides: Characterization, preparation and photocatalytic properties-A review. *Applied Catalysis B: Environmental*, *186*, 97–126.
- Tang, L., Feng, C., Deng, Y., Zeng, G., Wang, J., Liu, Y., Feng, H., & Wang, J. (2018). Enhanced photocatalytic activity of ternary Ag/g-C₃N₄/NaTaO₃ photocatalysts under wide spectrum light radiation: The high potential band protection mechanism. *Applied Catalysis B: Environmental*, *230*, 102–114.
- Fu, Z., Zhang, S., & Fu, Z. (2019). Hydrothermal preparation of NaTaO₃/rGO composite photocatalyst to enhance UV photocatalytic activity. *Results Phys*, *15*, 102669.
- Zhang, P., Dong, Z., Ran, Y., Xie, H., Lu, Y., & Ding, S. (2018). Preparation and photocatalytic application of AgBr modified Bi₂WO₆ nanosheets with high adsorption capacity. *Journal of Materials Research*, *33*, 3953–3962.
- Sharma, S., Dutta, V., Raizada, P., Hosseini-Bandegharai, A., Thakur, V. K., Kalia, S., Nguyen, V. H., & Singh, P. (2021). Recent advances in silver bromide-based Z-scheme photocatalytic systems for environmental and energy applications: A review. *Journal of Environmental Chemical Engineering*, *9*, 105157.
- Senthil, R. A., Wu, Y., Liu, X., & Pan, J. (2021). A facile synthesis of nano AgBr attached potato-like Ag₂MoO₄ composite as highly visible-light active photocatalyst for purification of industrial waste-water. *Environmental Pollution*, *269*, 116034.
- Tang, L., Wang, J. J., Wang, L., Jia, C. T., Lv, G. X., Liu, N., & Wu, M. H. (2016). Facile synthesis of silver bromide-based nanomaterials and their efficient and rapid selective adsorption mechanisms toward anionic dyes ACS Sustain. *Chemical Engineering*, *4*, 4617–4625.
- Liang, S., Zhang, D., Yao, X., Han, R., Zhang, Q., Jin, C., Pu, X., & Geng, Y. (2020). Deposition-precipitation synthesis of Yb³⁺/Er³⁺ co-doped BiOBr/AgBr heterojunction photocatalysts with enhanced photocatalytic activity under Vis/NIR light irradiation. *Separation and Purification Technology*, *238*, 116450.
- Puga, F., Navío, J. A., & Hidalgo, M. C. (2021). Enhanced UV and visible light photocatalytic properties of synthesized AgBr/SnO₂ composites. *Separation and Purification Technology*, *257*, 117948.
- Sánchez-Cid, P., Jaramillo-Páez, C., Navío, J. A., Martín-Gómez, A. N., & Hidalgo, M. C. (2019). Coupling of Ag₂CO₃ to an optimized ZnO photocatalyst: Advantages vs. disadvantages. *Journal of Photochemistry and Photobiology A: Chemistry*, *369*, 119–132.
- Shi, J., Liu, G., Wang, N., & Li, C. (2012). Microwave-assisted hydrothermal synthesis of perovskite NaTaO₃ nanocrystals and their photocatalytic properties. *Journal of Materials Chemistry*, *22*, 18808–18813.
- Huang, L., Chan, Q., Zhang, B., Wu, X., Gao, P., Jiao, Z., & Liu, Y. (2011). Preparation of sodium tantalate with different structures and its photocatalytic activity for H₂ evolution from water splitting, Chinese. *Journal of Catalysis*, *32*, 1822–1830.
- Sing, K. S. W. (1982). Reporting physisorption data for gas/solid systems. *Pure and Applied Chemistry*, *54*, 2201–2218.
- Senthil, R. A., Osman, S., Pan, J., Sun, M., Khan, A., Yang, V., & Sun, Y. (2019). A facile single-pot synthesis of WO₃/AgCl composite with enhanced photocatalytic and photoelectrochemical performance under visible-light irradiation. *Colloids Surfaces A Physicochem. Eng. Asp.*, *567*, 171–183.
- Arumugam Senthil, R., Khan, A., Pan, J., Osman, S., Yang, V., Kumar, T. R., Sun, Y., & Liu, X. (2020). A facile single-pot synthesis of visible-light-driven AgBr/Ag₂CO₃ composite as efficient photocatalytic material for water purification. *Colloids and Surfaces A Physicochemical and Engineering Aspects*, *586*, 124183.
- Li, X., & Zang, J. (2011). Hydrothermal synthesis and characterization of Lanthanum-doped NaTaO₃ with high photocatalytic activity. *Catalysis Communications*, *12*, 1380–1383.

27. Gu, X., Lu, H., Kan, C., & Yao, J. (2015). One-pot hydrothermal synthesis of zeolite/sodium tantalate composite and its photodegradation of methyl orange. *Materials Research Bulletin*, *68*, 185–188.
28. Hu, H., & Fu, Y. (2020). Surfactant-assisted hydrothermal synthesis of NaTaO₃ nanotubes with enhanced photodegradation activity. *Micro. Nano Letters*, *15*, 370–373.
29. Yang, S., Xu, D., Chen, B., Luo, B., Yan, X., Xiao, L., & Shi, W. (2016). Synthesis and visible-light-driven photocatalytic activity of p-n heterojunction Ag₂O/NaTaO₃ nanocubes. *Applied Surface Science*, *383*, 214–221.
30. Yang, F., Yan, L., Zhang, B., He, X., Li, Y., Tang, Y., Ma, C., & Li, Y. (2019). Fabrication of ternary NaTaO₃/g-C₃N₄/G heterojunction photocatalyst with enhanced activity for Rhodamine B degradation. *Journal of Alloys and Compounds*, *805*, 802–810.
31. Yin, H., Zhang, M., Yao, J., Luo, Y., Li, P., Liu, X., & Chen, S. (2020). Surfactant-assisted synthesis of direct Z-scheme AgBr/β-Ag₂WO₄ heterostructures with enhanced visible-light-driven photocatalytic activities. *Materials Science in Semiconductor Processing*, *105*, 104688.
32. Chen, W., Wilmet, M., Truong, T. G., Dumait, N., Cordier, S., Matsui, Y., Hara, T., Takei, T., Saito, N., Nguyen, T. K. N., Ohsawa, T., Ohashi, N., Uchikoshi, T., & Grasset, F. (2018). Embedding hexanuclear tantalum bromide cluster Ta₆Br₁₂ into SiO₂ nanoparticles by reverse microemulsion method. *Heliyon*, *4*, e00654.
33. Xu, D., Shi, W., Yang, S., Chen, B., Bai, H., & Xiao, L. (2016). Fabrication of ternary p-n heterostructures AgCl/Ag₂O/NaTaO₃ photocatalysts: Enhanced charge separation and photocatalytic properties under visible light irradiation. *Catalysis Communications*, *84*, 163–166.
34. Puga, F., Navío, J. A., Paulete-Romero, M. A., Córdoba, J. M., & Hidalgo, M. C. (2022). Exploring the photocatalytic activities of a highly 001 faceted TiO₂ sensitized by coupling with AgBr or Ag₃PO₄. *Materials Science and Engineering B*, *276*, 1–13.
35. Liu, X., Zhang, D., Guo, B., Qu, Y., Tian, G., Yue, H., & Feng, S. (2015). Recyclable and visible light sensitive Ag-AgBr/TiO₂: Surface adsorption and photodegradation of MO. *Applied Surface Science*, *353*, 913–923.
36. Yeh, M. Y., Lin, C., Vu, C. T., Hsu, K. F., Lee, S. Y., Li, W. R., & Yen, C. F. (2017). Post-calcination effects of sodium tantalate synthesized by microwave-assisted hydrothermal method and its photocatalytic performance under UV and visible light. *Materials Research Bulletin*, *90*, 182–187.
37. Liu, X. H., Luo, X. H., Lu, S. X., Zhang, J. C., & Cao, W. L. (2007). A novel cetyltrimethyl ammonium silver bromide complex and silver bromide nanoparticles obtained by the surfactant counterion. *Journal of Colloid and Interface Science*, *307*, 94–100.
38. Ulhaq, I., Ahmad, W., Ahmad, I., Yaseen, M., & Ilyas, M. (2021). Engineering TiO₂ supported CTAB modified bentonite for treatment of refinery wastewater through simultaneous photocatalytic oxidation and adsorption. *J. Water Process Eng.*, *43*, 102239.
39. Erady, V., Mascarenhas, R. J., Satpati, A. K., Bhakta, A. K., Mekhalif, Z., Delhalle, J., & Dhason, A. (2019). Carbon paste modified with Bi decorated multi-walled carbon nanotubes and CTAB as a sensitive voltammetric sensor for the detection of Caffeic acid. *Microchemical Journal*, *146*, 73–82.
40. Puga, F., Navío, J. A., Córdoba, J. M., Romero-Sarria, F., & Hidalgo, M. C. (2022). Insights into the structural and physicochemical properties of Zn-Bi-O composites for efficient photodegradation of caffeic acid, rhodamine B and methyl orange. *Applied Surface Science*, *581*, 152351.
41. Le Person, A., Lacoste, A. S., & Cornard, J. P. (2013). Photodegradation of trans-caffeic acid in aqueous solution and influence of complexation by metal ions. *Journal of Photochemistry and Photobiology. A: Chemistry*, *265*, 10–19.
42. Alig, A. R. G., Gourdon, D., & Israelachvili, J. (2007). Properties of confined and sheared rhodamine B films studied by SFA-FECO spectroscopy. *The Journal of Physical Chemistry B*, *111*, 95–106.
43. Setiawan, D., Kazaryan, A., Martoprawiro, M. A., & Filatov, M. (2010). A first principles study of fluorescence quenching in rhodamine B dimers: How can quenching occur in dimeric species? *Physical Chemistry Chemical Physics: PCCP*, *12*, 11238–11244.
44. Cheng, Q., Wang, C., Doudrick, K., & Chan, C. K. (2015). Hexavalent chromium removal using metal oxide photocatalysts. *Applied Catalysis B: Environmental*, *176–177*, 740–748.
45. Yao, S., Xue, S., Zhang, J., & Shen, X. (2016). Characterization and mechanism analysis of AgBr mixed cuboid WO₃ rods with enhanced photocatalytic activity. *RSC Advances*, *6*, 93436–93444.
46. Wang, F., Wang, T., Lang, J., Su, Y., & Wang, X. (2017). Improved photocatalytic activity and durability of AgTaO₃/AgBr heterojunction: The relevance of phase and electronic structure. *Journal of Molecular Catalysis A: Chemical*, *426*, 52–59.
47. Deng, Y., Chen, Y., Chen, B., & Ma, J. (2013). Preparation, characterization and photocatalytic activity of CuBi₂O₄/NaTaO₃ coupled photocatalysts. *Journal of Alloys and Compounds*, *559*, 116–122.
48. C. Xu, P. Ravi Anusuyadevi, C. Aymonier, R. Luque, S. Marre, Nanostructured materials for photocatalysis, *Chemical Society Review* *48* (2019)
49. Duan, C., Song, J., Wang, B., Li, L., Wang, R., & Zhang, B. (2019). Lactic Acid Assisted Solvothermal Synthesis of BiOCl_{1-x}I_x Solid Solutions as Excellent Visible Light Photocatalysts. *Chem. Res. Chinese Univ.*, *35*, 277–284.
50. Nosaka, Y., & Nosaka, A. Y. (2017). Generation and Detection of Reactive Oxygen Species in Photocatalysis. *Chemical Reviews*, *117*, 11302–11336.
51. Zhang, Z., Yu, Y., & Wang, P. (2012). Hierarchical top-porous/bottom-tubular TiO₂ nanostructures decorated with Pd nanoparticles for efficient photoelectrocatalytic decomposition of synergistic pollutants. *ACS Applied Materials & Interfaces*, *4*, 990–996.
52. Weldegebrieal, G. K., & Sibhatu, A. K. (2021). Photocatalytic activity of biosynthesized α-Fe₂O₃ nanoparticles for the degradation of methylene blue and methyl orange dyes. *Optik (Stuttg.)*, *241*, 167226.
53. Wang, X., Ma, J., Kong, Y., Fan, C., Peng, M., & Komarneni, S. (2019). Synthesis of p-n heterojunction Ag₃PO₄/NaTaO₃ composite photocatalyst for enhanced visible-light-driven photocatalytic performance. *Materials Letters*, *251*, 192–195.
54. Singh, A. P., Kumar, S., & Thirumal, M. (2019). Efficient Charge Transfer in Heterostructures of CdS/NaTaO₃ with Improved Visible-Light-Driven Photocatalytic Activity. *ACS Omega*, *4*, 12175–12185.
55. Li, H., Shi, X., Liu, X., & Li, X. (2020). Synthesis of novel, visible-light driven S, N-doped NaTaO₃ catalysts with high photocatalytic activity. *Applied Surface Science*, *508*, 145306.
56. Xu, D., Chen, M., Song, S., Jiang, D., Fan, W., & Shi, W. (2014). The synthesis of a novel Ag-NaTaO₃ hybrid with plasmonic photocatalytic activity under visible-light. *CrystEngComm*, *16*, 1384–1388.